The Vortex Field Behind A Single And Tandem Flapping Airfoil

David S. Nobes[1,*], Mathew Bussiere [1] and C. Robert Koch [1]

[1]Department of Mechanical Engineering, University of Alberta, Edmonton, Canada
*corresponding author: david.nobes@ualberta.ca

Abstract
The wake of a NACA 0012 airfoil oscillating sinusoidal about its aerodynamic center in a general co-flow generates a well-known characteristic vortex street. The introduction of vorticity into the flow in a controlled way could be used as a means to either enhance or dampen any large-scale motion present. The oscillating aerofoil can then be seen as the actuation component of an active control system. To investigate the potential of using a flapping wing as an actuation device the flow field that it generates first needs to be characterized. This can then be used to affect a fluctuating flow field, which in this case is the vortex field generated by an identical oscillating airfoil downstream from the first. Flow visualization coupled with particle image velocimetry is used to investigate and characterize the flow field from both a single oscillating airfoil and the interacting flow field between two tandem airfoils. The relative phase between the two wings is adjusted to investigate how the vorticity field is either enhanced or reduced by the added vorticity from the second aerofoil. A combinatorial vortex detection and characterization algorithm is implemented to identify vortices within the field and their development as they are advect downstream from the tandem aerofoils. Flow features present over a range of conditions as well as quantitative information defining the vorticity field show that the hindfoil in the tandem setup can be used to affect the characteristics of a large-scale vortex.

Keywords: vortex generation, combinatorial vortex detection, flow visualization, particle image velocimetry, flow control

1 Introduction

For many fluid flow applications vortices and large-scale fluid structures are essential and important flow features. They can dominate the flow and are important mixing and transport phenomenon within the flow field. These are typically identified as spatially coherent structures that can be temporary evolving and are often identified under a single heading as a vortex [1]. Manipulation and control of these phenomena potentially has the ability to allow the introduction of control strategies for manipulating the fluid process. To undertake this, methods are needed for identifying these phenomena within the flow and for either enhancing or destroying the phenomena. With these elements active control of the fluid process could be implemented.

A number of different approaches can be used to generate large scale vortical flow features. These include mechanical devices such as a pitching airfoil [2] and biological devices used for propulsion [3][4]. To allow a detailed development and understanding of how vortices and large-scale phenomenon can be controlled, a well-defined and controllable device for generating these features is needed. To do this a NACA 0012 airfoil was aligned in a uniform flow field of water and oscillated in a sinusoidal manner about its aerodynamic centre. This device was used as it generates a consistent vertical wake allowing the development of strategies for detection and characterization of flow structures [2][5]. The wake scheme that is generated for a given Reynolds number can be described by the vortex position and orientation within the wake [3]. A wide range of flow conditions can be summarized using a phase diagram that maps important wake features as a function of two independent dimensionless parameters. These are typically the Strouhal number based on the flapping frequency and dimensionless amplitude based on the cord length [3][7]. A number of other important parameters for characterizing these flow features include the coordinates of the vortex core, the vortex drift velocity, the maximum vorticity, vortex circulation, radius of the vortex and maximum circumferential velocity also need to be defined [8]. All of these parameters can be reliably determined from spatially correlated measurement of the velocity field.

The aim of this paper is to investigate how large-scale feature in the flow, a vortex, can be manipulated using a device that can generate a precise amount of vorticity. To undertake this a known vortex will be generated using an aerofoil (forefoil) which will then interact with the actuation device (hindfoil) to manipulate the incoming vortex. The vorticity field of this tandem arrangement of aerofoils is studied first by

characterizing the vortex field generated by a single aerofoil using flow visualization. Quantitative measurement of the 2-D flow field is then carried out using particle image velocimetry (PIV). The interacting wakes are then investigated using PIV to visualize the vortex wake and to provide a quantitative measure of the interacting vortex field and investigate how the hindfoil can be used to either enhance or destroy the incoming vortex.

2 Experimental methodology

2.1   General flow facility

The flow facility used to develop the general flow in all experiments is an open re-circulating water channel with a cross-section of a 0.7x0.4 m (27.5"x16") and low turbulence characteristics [9]. The center of the channel test section is located 3100 mm downstream from the inlet turbulence grid at the inlet of the water channel and consists of flat stainless steel bars that have a total open area of 56%. The turbulence grid generates a uniform streamwise velocity profile with variations of 5% and turbulence intensity for the mean horizontal of 4% at the test section [9]. An orifice plate flow meter in the return section is used to bulk characterize the volume flow rate, $\dot{Q}$ in the water channel.

2.2   The oscillating airfoil apparatus

To oscillate the airfoil in a controlled manner a stepper motor (PK258-02Dl, Oriental Motor) coupled to a driveshaft on the aerodynamic center of the airfoil was used. The aluminum airfoil was constructed from a continuous extrusion with a cross-sectional NACA 0012 shape and a chord length C = 75mm. The airfoil was suspended vertically such that it hangs down through the free surface into the water channel, perpendicular to the upstream flow direction. A real-time control system (dSPACE) controlled the stepper motor motion using custom software and provided output trigger signals when the airfoil pitch met a desired angle. In this manner, the imaging system could reliably collect data at prescribed positions allowing for both phase averaged and time averaged data sets.
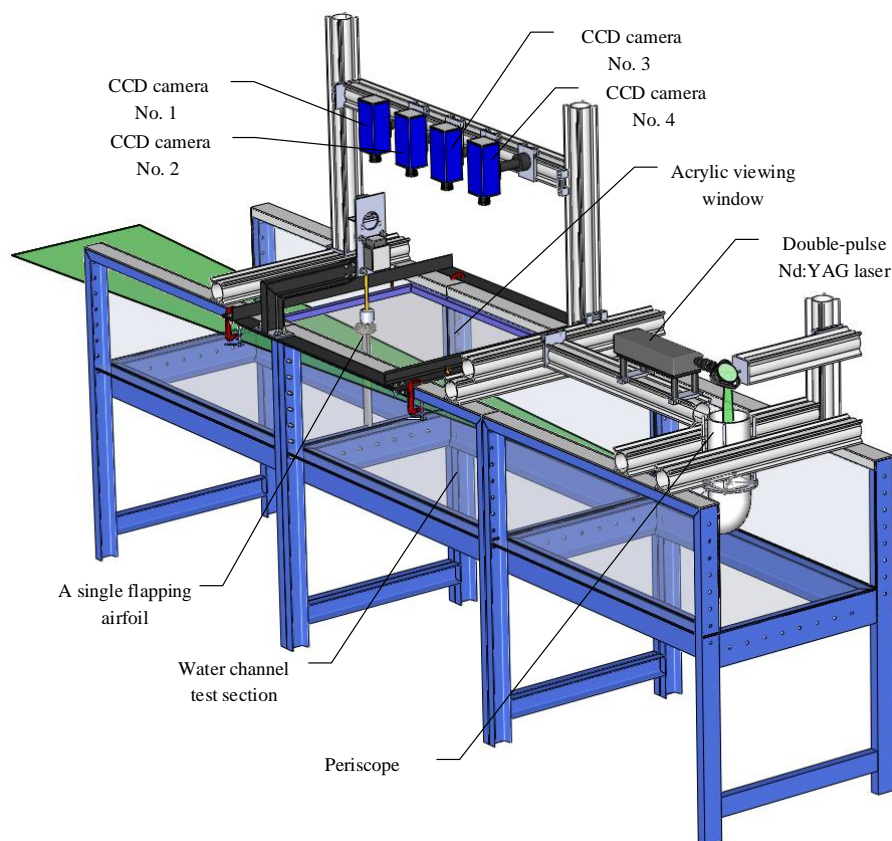
2.3   Flow imaging system

Fig. 1 The typical arrangement for all imaging equipment in relation to the test section

A schematic of the typical imaging system in relation to the water channel test section used in all experiments is shown in Fig. 1. The region of interest (ROI) in the test section was imaged by four 2,112×2,072 pixel resolution, 14-bit duel-frame CCD cameras (Imager Pro X 4M, LaVision) viewing the investigation plane through 4 independent local coordinate systems. An acrylic sheet was place on the free surface and cameras imaged through it to remove surface refraction effects. A double-pulse Nd:YAG laser (Solo III-15z, New Wave) illuminated the ROI which was seeded with 18μm hollow glass spheres (Sphericel 018, Potters Industries) for PIV measurements. The laser beam was focused into a thin sheet which was directed upstream by a mirror and submerged periscope. Calibration of the images generated by the cameras is used to map data from pixel space to real space and to remove optical and perspective distortion. Calibration is performed using a custom 300 mm × 800 mm 2D calibration target. The target is comprised of equally spaced black dots 1.3 mm in diameter and spaced 3 mm on a square lattice. The calibration target was placed into the water channel such that its surface is coincident with the ROI [10].

2.4   Vector Processing

Processing of image data into vector field consisted of a number of steps. Prior to cross-correlation of the image pairs, the raw images were preprocessed with commercial software (LaVision GmbH, DaVis 8.05). This step gives rise to enhanced particle intensity and shape and ultimately leads to better correlation [11][12]. The correlation strength is affected by disparity in the image intensity arising from light sheet non-uniformities, shadows, reflections or variations in particle size [11]. In this work, correlation strength was improved with the following image pre-processing methods: background intensity subtraction, sliding minimum subtraction and min-max filter for intensity normalization.

In general, the vector fields obtained directly from the cross-correlation needed to be smoothed and verified before other parameters such as vorticity and streamlines are calculated [13]. The vector fields were post-processed with commercial PIV software (LaVision GmbH, DaVis 8.05) and mathematical software (Mathworks Inc, Matlab). Vector field post-processing automatically detects and replaces spurious vectors and generates a smooth field for future computation of derived quantities and statistical values [11]. A median test rejects vectors whose magnitude or components of magnitude exceed a certain threshold when compared to the median of neighboring vectors [11][14]. The four individual vector fields obtained from each camera were reassembled into one global coherent vector field with custom code [10] developed with commercial mathematics software (Mathworks Inc, Matlab). Gaussian smoothing was only applied once and all four vector fields were stitched ensuring smooth transitions at the seams where the individual fields overlap.

2.5   Experiment configurations of the oscillating airfoil

Two types of experiments were undertaken to visualize the flow and to measure the velocity field for either a single or a tandem airfoil configuration. These different airfoil configurations are shown in Fig. 2. To visualize the flow dense slurry composed of glass spheres (18μm diameter hollow glass spheres for PIV seeding) and water is injected through 2 small visualization ports on either side of the airfoil at the quarter chord distance as shown in Fig. 2(a). The slurry is contained in a reservoir located at a height, h above the visualization ports. The visualization ports are located 100 mm beneath the free surface and the reservoir height, h is adjusted such that the velocity at which the slurry leaves the ports is virtually identical to that of the fluid passing over the airfoil's surface at that location. In this manner the streaklines generated from the slurry are as laminar as possible. To characterize the flow, instantaneous wake images were taken with the four overhead CCD cameras. The laser sheet light scatters off the dense slurry and into the four CCD cameras. The images were stitched together with calibrated offsets to produce one single image with a global coordinate system with its origin at the trailing edge of the airfoil. These images were visually inspected and the wake type for each identified.

For both configurations of single and tandem aerofoil PIV measurements were carried out. The bulk flow of the water channel was seeded with 18μm hollow glass spheres to mark the fluid motion. The laser sheet was also located 100 mm beneath the free surface region where the wake had been identified to be two-dimensional. The aim here was to minimize the distance below the surface improve imaging of the velocity field. Image sets were collected over a range of frequency and amplitude conditions to allow broad investigation of the generated flow fields.
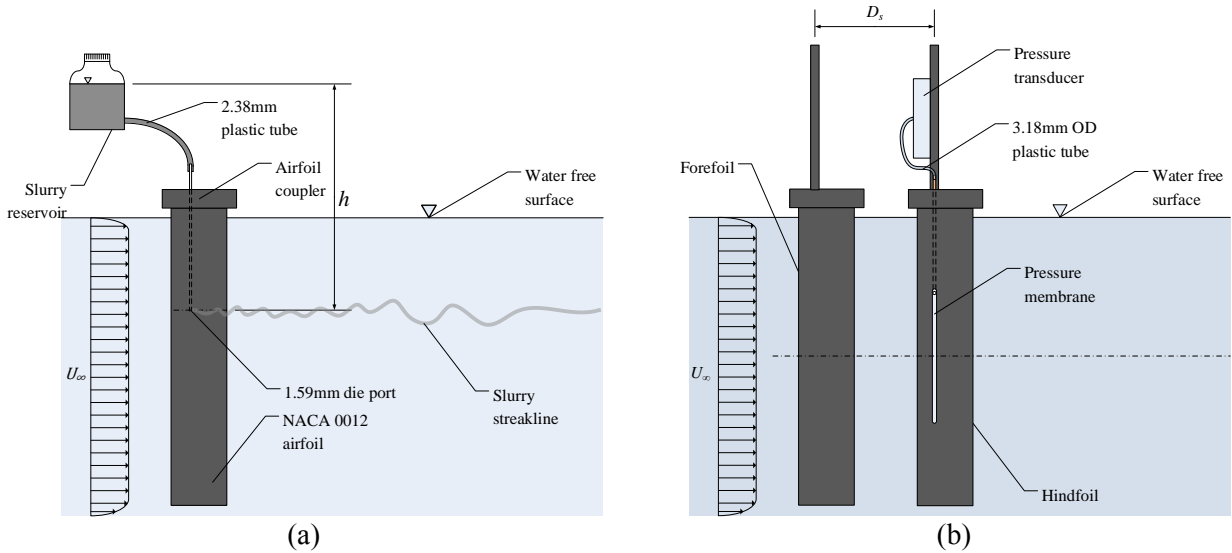
Fig. 2 Side view schematics of the two configurations investigated: (a) the single airfoil and (b) the tandem airfoils.

2.6   Measurement uncertainties

An estimation of the PIV measurement uncertainty is used to assess the final accuracy of the measured velocity field. The individual components of the PIV system each contribute to the overall uncertainty in the system. Uncertainty arises from the ability of the seed particle motion to represent local fluid motion. This uncertainty is due to particle slip in which the velocity of the seed particles (*v*) lag behind the fluid motion (*u*) by some finite quantity. The slip velocity is computed to first order by [14]:

$$|v - u| = \left[\frac{(\bar{\rho} - 1)g\tau_o}{\bar{\rho}} \right] \qquad (1)$$

with gravitational constant $g = 9.81 \text{m/s}^2$, $\bar{\rho}$ is the density ratio taking into account the density of the seed particle $\rho_p = 600 \text{kg/m}^3$ and the density of water $\rho_w = 998 \text{kg/m}^3$ such that:

$$\bar{\rho} = \rho_p / \rho_w \qquad (2)$$

and a time constant:

$$\tau_o = \frac{\rho_p d_p^2}{18 \nu_w \rho_w} \qquad (3)$$

where $d_p = 18 \mu\text{m}$ is the diameter of the particle and $\nu_w = 1.004 \times 10^6 \text{m}^2/s$ is the kinematic viscosity of water.

A slip velocity error of 0.47% relative to the freestream velocity of $u = U_\infty = 0.017 \text{m/s}$ is approximated to first order with (1). Uncertainty due to varying image magnification over the image domain is corrected by calibrating with a calibration target; however, image magnification also varies over the thickness of the light sheet and the associated magnification uncertainty is on the order of 0.3% for most PIV arrangements [14]. The measurement uncertainty in determining the location of the correlation peak for a 8 pixel particle displacement is about 1-2% of the full scale velocity for similar planar PIV systems [14][15]. Uncertainty in the timing of events has a resolution of 10 ns and a jitter of less than 1 ns. [15]. The overall uncertainty is estimated to be 2%.

3 Detection of a vortex in a wake

The basic concepts and approaches to vortex detection that can be used in developing an algorithm can be explored by reviewing three vortex detection methods that have been used in the literature. These are the maximum vorticity (MV) method [16], the cross sectional lines (CSL) method [8] and the winding angle (WA) method [17]. In this study these have been combined into a combinatorial vortex detection (CVD) method for determining vortex characteristics from PIV data. A flow chart of this method is shown in Fig. 3(a) and a complete discussion of its development can be found in [10][18]. An aim of the CVD method was that it must consistently detect and characterize multiple vortices from PIV generated velocity vector maps. It must label each vortex (*i*) in the flow field in Fig. 3(b) and locate the vortex cores (x_i, y_i), the drift velocity

$\vec{v}_{drift} = (v_{drift,x}, v_{drift,y})$, the circulation Γ_i, the peak vorticity ω_{peak} and boundary radii, r_v of the individual vortical structures. Ultimately, the method must reduce the size of the original dataset by accurately conserving important vortex parameters which can then be used to character the generated wake.
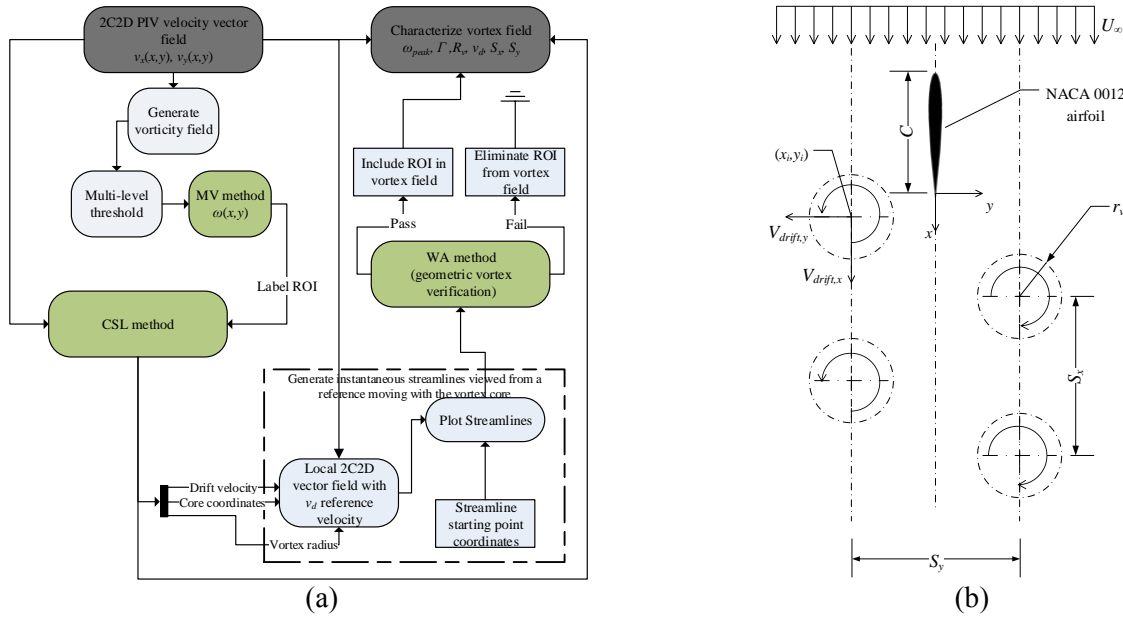

Fig. 3 (a) A flowchart of the combination of three vortex detection methods into a combinatorial vortex detection (CVD) method (b) schematic showing the definition of the parameters determined from the CVD.

4 The wake of a single flapping wing

The wake generated by the oscillation of the airfoil is essentially 2D and is comprised of coherent structures which separate from the trailing edge of the airfoil and travel downstream at a given drift velocity. The complex wake flow can be parameterized by:

- The spatial arrangement of vortices in the wake
- The spatial coordinates (x_i, y_i) of vortex cores relative to the airfoil
- The vortex size, r_v defined by a circle fitted to the vortex
- The vortex drift velocity , $\vec{v}_{drift} = (v_{drift,x}, v_{drift,y})$
- Core region circulation of individual vortices, Γ
- The peak vorticity of individual vortices, ω_{peak}

These parameters are a complex function of the airfoil's angular oscillation waveform amplitude θ_A, frequency f and the Reynolds number Re, defined as:

$$Re = \frac{U_\infty D}{\nu} \tag{4}$$

For experiments performed in this study, the free stream velocity U_∞ is held constant at 17 mm/s with an airfoil thickness of $D = 8.6$ mm and kinematic viscosity of water is $\nu = 1 \times 10^{-6}$ m^2/s so that $Re = 146$. The airfoil of chord length, C was limited to small pitch oscillation amplitudes ($\theta_A \leq 8°$) to prevent the creation of leading edge vortices, which would appear in the wake. The oscillation waveform is described by $\theta_{af}(t) = (\theta_A/2)\sin(2\pi f t)$ and several wake conditions are achieved by changing the oscillation amplitude θ_A and frequency f.
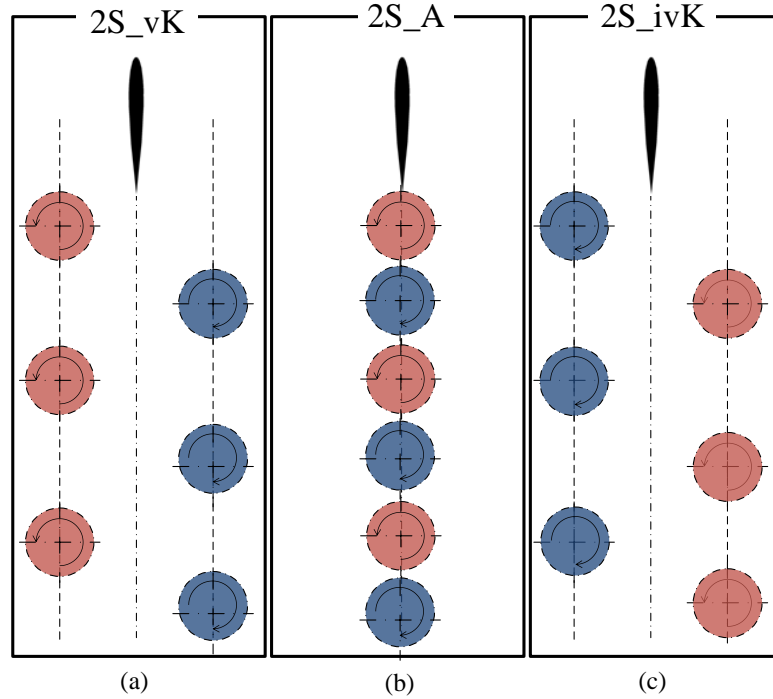
Fig. 4 A schematic of the main types of vortex arrangements generated in the wake of a flapping airfoil [10].

The vortex field generated in the wake can be divided into categories based on its spatial arrangement. Fig. 4 shows the various vortex wake categories where the blue circles represent vortices with positive counter-clockwise (CCW) rotation and those in red represent vortices with negative clock-wise (CW) rotation. A von Karman wake (2S_vK) is show in Fig. 4(a) and is defined by two vortices of opposite rotation that are shed alternately every oscillation period [3]. This wake has two distinct rows of opposite signed vortices that are symmetric about the airfoil chord line. At a set amplitude with increasing flapping frequency, the lateral vortex spacing, S_y (Fig. 3b) decreases until a unique condition is achieved where the vortices align in the wake of the airfoil as is show in Fig. 4(b) and is classified as an aligned wake (2S_A). A further increase in flapping frequency for a constant amplitude will generate an inverted von Karman wake (2S_ivK) which is shown in Fig. 4(c). This is defined as a von Karman wake in which the sign of vorticity in each of the two rows is reversed. These three wake schemes are the focus of this study and belong to the 2S family meaning that only two single vortices are shed per oscillation cycle of the airfoil.

The wake of an oscillating airfoil is dependent on the harmonic motion of the airfoil [7]. A 2D airfoil performing both periodic heaving and pitching motions with an arbitrary oscillation waveform can have an extremely complicated three dimensional wake. Heaving is where the aerodynamic centre of the airfoil moves perpendicular to the free stream flow, while pitching is when the airfoil's angle of attack is changed. Airfoil motion limited to sinusoidal pitch oscillations was investigated in this study and can be characterized by [3] the Reynolds number defined in (4) and a thickness based Strouhal number:

$$St_d = \frac{fD}{U_\infty} \tag{6}$$

where *f* is the frequency of pitching oscillation and a dimensionless amplitude of oscillation:

$$A_d = A/D \tag{7}$$

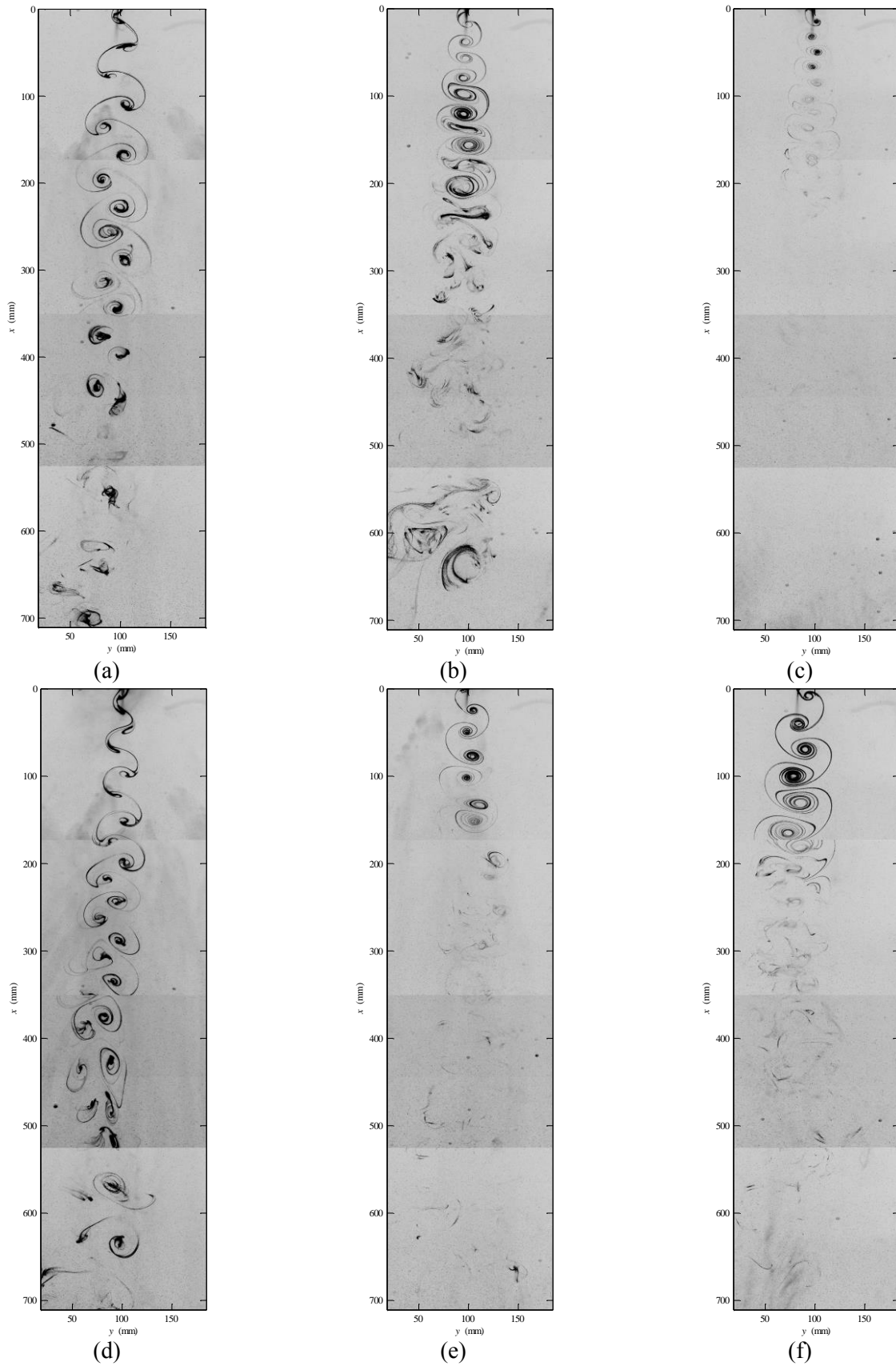where *A* is the linear oscillating amplitude of the training edge.

Fig. 5 Instantaneous streakline images for a constant $A_d = 0.84$ and a) $St_d = 0.129$ a 2S_vK type wake, b) $St_d = 0.201$ a 2S_A type wake, c) $St_d = 0.274$ a 2S_ivK type wake. Also, instantaneous streakline image for a constant $St_d = 0.161$ and a) $A_d = 0.42$ a 2S_vK type wake, b) $A_d = 1.04$ a 2S_A type wake and c) $A_d = 1.47$ a 2S_ivK type wake.

Characterizing the wake behind an oscillating NACA 0012 and investigating the effect of changing both frequency f and amplitude θ_A of oscillation can be carried out using flow visualization techniques using instantaneous imaging of the flow. These images require minimal processing since they are visually interpreted. Select examples of instantaneous wake images are shown in Fig. 5(a-f). These images capture the three primary wake types under investigation: the 2S_vK wake Fig. 5(a,d), the 2S_A wake Fig. 5(b,e) and the 2S_ivK wake Fig. 5(c,f). The three wake types in Fig. 5(a-c) are achieved by varying the frequency of oscillation f while maintaining constant amplitude of $A_d = 0.84$. The three wake types can also be achieved by varying the amplitude of oscillation as shown in Fig. 5(d-f) while maintaining a constant frequency of $St_d = 0.161$. The images show the vortices and how they are arranged in the wake. Lines linking the individual vortices, called connecting braids [2], are visible in the images. The braids reveal the direction of rotation of the vortices and allow the associated wakes type to be identified. As the vortices progress downstream they grow in diameter and the particle slurry diffuses into the surrounding fluid making the vortices increasingly less visible. While difficult to compute the rate or exact magnitudes of vortex decay from the images quantitatively, it appears that the vortices decay much faster in the 2S_A and 2S_ivK when compared to the 2S_vK.

The values for θ_A, f, St_d , A_d and the corresponding wake type for 37 test cases [10] captured using flow visualization are determined. The images are then divided into 3 types of wakes: 2S_vK, 2S_A, and 2S_ivK based on visual inspection. A phase map in Fig. 6 is a graphical representation of the data collected. The individual wake types are plotted with dimensionless frequency St_d as the horizontal axis and dimensionless amplitude A_d as the vertical axis. This phase map serves to predict important transitions between the 3 wake types and demonstrates how variations in St_d and A_d affect the spatial organization of large structures in the wake of an oscillating airfoil. Also identified in the figure are the wakes corresponding to the images shown in Fig. 5. The 2S_A wake type may be viewed as a transitional region where the 2 vortex rows coincide. 2S_A wake types are marked as black squares '□' and the transitional region is estimated by a spline curve fit between these points. This curve tends to a minimum of $A_d = 0.42$ indicating that below this oscillation amplitude, the wake type is 2S_vK for all oscillation frequencies. The 2S_vK to 2S_ivK transition curves obtained by [3] and by [7] are compared to the one obtained in this study. The curve from [3] shows good agreement throughout, whereas the curve from [7] only shows good agreement for $St_d < 0.175$. This is attributed to an insufficient number of data points in the range of $0.4 < A_d < 0.6$ for the study reported in [7].
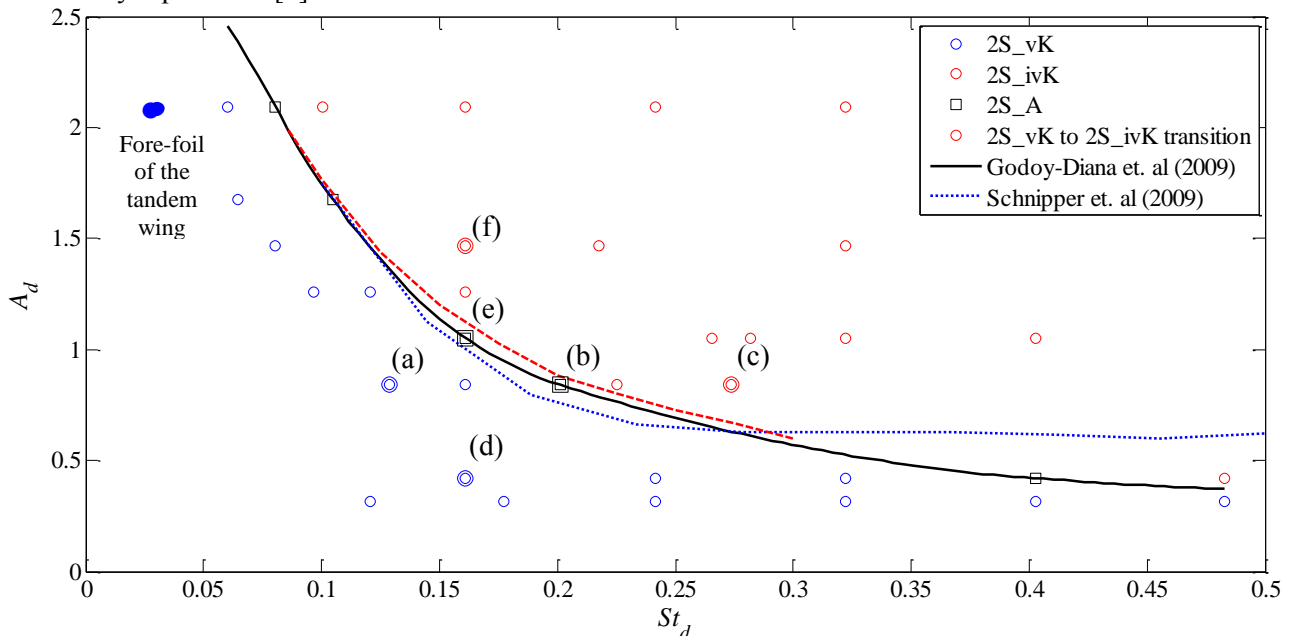

Fig. 6 Dimensionless Strouhal number St_d based on chord width D, and dimensionless amplitude A_d map out various wake patterns which are the result of several oscillation frequency and amplitude combinations for the NACA 0012 airfoil in steady flow. The black dotted line indicates the boundary where the wake transitions from a 2S_vK to an 2S_ivK wake and the purple dotted line indicates where the wake transitions from 2S_ivK to 2S_ivKa.

5 Vortex generation from a single airfoil (forefoil)

Before studying the interacting wake characteristics of a tandem airfoil system in the region behind the hindfoil, it is first necessary to isolate the forefoil and investigate its wake characteristics independent of the presence of the hindfoil. This creates a reference point from which to compare future tandem wing results and the selected condition is highlighted on the phase map in Fig. 6. In Fig. 7(a) a sample vorticity field of the single airfoil with oscillation frequency and amplitude of 4 rad/s and $\theta_A = 20°$ is shown compared to a phase averaged vorticity field of 100 instantaneous measurements shown in Fig. 7(b). This correspond to St_d = 0.03 and A_d = 2.089 as highlighted in Fig. 6. There are 6 vortices shed per oscillation cycle, two primary vortices of opposite rotation each surrounded by two same signed vortices of lesser strength. This wake is characterized by 2P+2S_vK [3] as the primary vortices are organized in a 2S_vK configuration. The total contribution of circulation Γ_{total} from all the vortices in a wake with N_{vtx} vortices of individual circulation Γ_i is defined by:

$$|\Gamma_{total}| = \sum_{i=1}^{N_{vtx}} |\Gamma_i| \tag{8}$$

For the wake in Fig. 7 the mean total contribution of circulation from all the vortices for each of the 100 wakes was $|\Gamma_{total,mean}| = 1.69×10^4$ mm²/s and will be compared to that of the various tandem wakes.
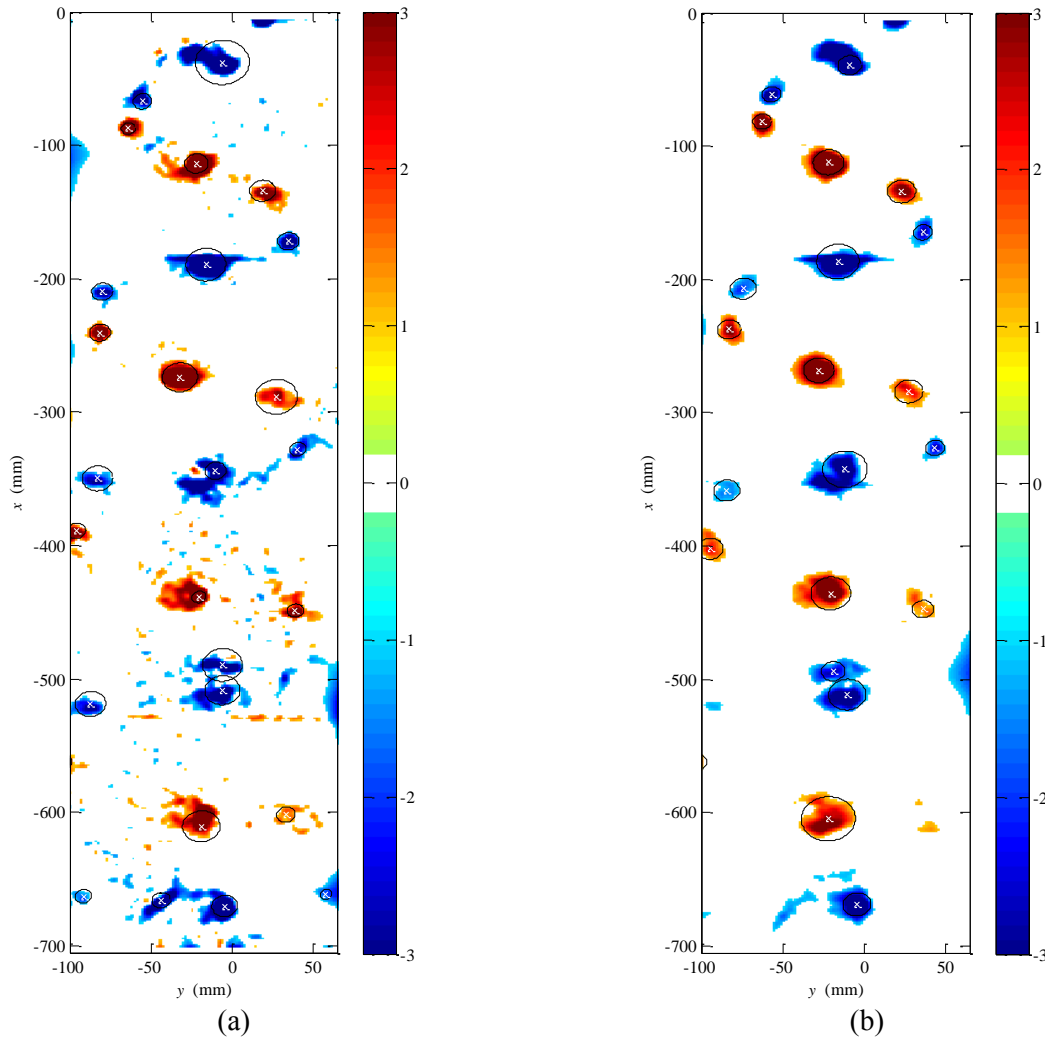

(a)   (b)

Fig. 7 Vorticity field for the wake of a single airfoil with oscillation frequency and amplitude of 4 rad/s and $\theta_A = 20°$ showing (a) a sample field showing and corresponding (b) phase averaged field. In addition, boundary radii for the detected vortices are shown black circles and the vortex cores are shown as white '×'. The circulation Γ $\left(\frac{mm^2}{s}\right)$ is shown in the colour map.

6 The interacting wake of a tandem wing

The interaction of the two wakes generated by a forefoil and hindfoil is measured using PIV to quantify vortex properties. Several adaptations to the basic single foil experimental setup were required for the tandem foil study. An identical geometry hindfoil was hung vertically into the water channel and downstream of the forefoil. They were separated by a distance D_c as defined in Fig. 8(a) along with other relevant parameters the tandem foil configuration. The angles $\theta_{ff}(t) = (\theta_A/2)\sin(2\pi f t)$ and $\theta_{hf}(t) = (\theta_A/2)\sin(2\pi f t - \Phi\pi/180°)$ expressed in degrees, correspond to the positive angle formed by the chord line and the wake centerline of the forefoil and the hindfoil respectively. Also, Φ is the phase lag of the hindfoil and θ_A is the pk-pk amplitude in degrees of the foils motion.

The ability to modify the properties of large coherent vortices in a 2S_vK wake with open-loop control is investigated by studying the effect of changing the phase of the hindfoil relative to the forefoil. Fig. 8(b) is a schematic of the anticipated interaction between the upstream 2S_vK wake generated by the forefoil and the sinusoidally forced hindfoil. An incoming upstream vortex interacts with the solid boundary of the hindfoil and the resulting wake downstream of the hindfoil is characterized with PIV measurements.
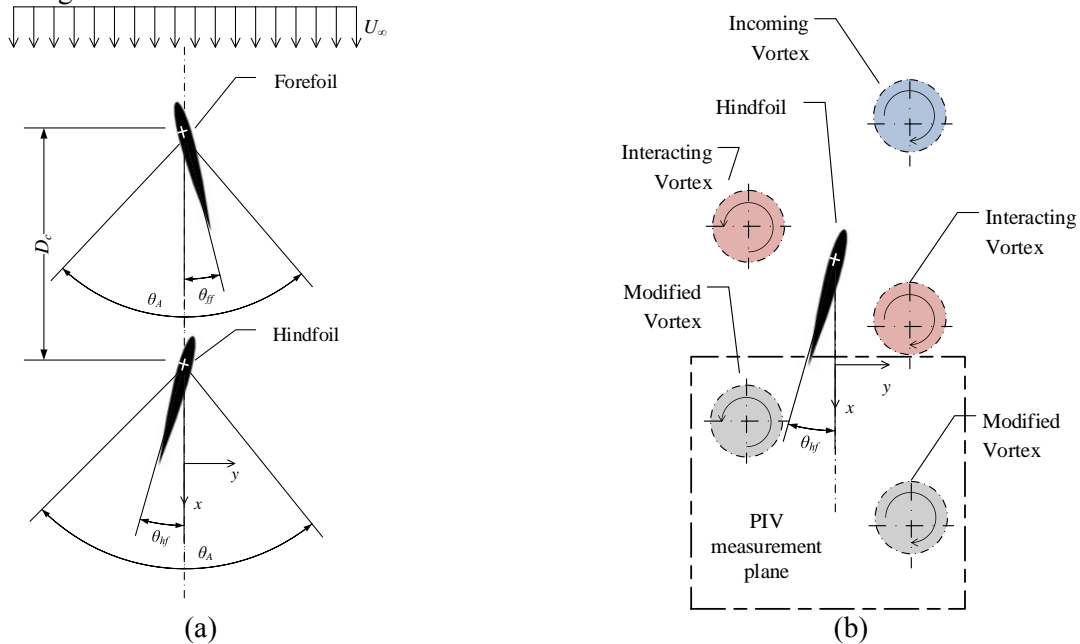

Fig. 8 Definitions of the tandem wing experiment, (a) the location of the forefoil and hindfoil in the flow field and (b) the location of the PIV measurement plane relative to the hindfoil.

6.1 Phase imaging of the tandem configuration

For each case, phase averaged vorticity field obtained from 100 individual hindfoil wakes are plotted in Fig. 9. This figure shows phases $\Phi = 0°$, $\Phi = 45°$, $\Phi = 90°$, $\Phi = 135°$, $\Phi = 180°$, $\Phi = 225°$, $\Phi = 270°$ and $\Phi = 315°$. The vorticity threshold used in the vortex detection is identical to that of the single airfoil case and remains constant throughout the various phases. A comparison with the single airfoil wake from Fig. 7 provides quantitative evidence that the presence of the second airfoil can substantially alter the wake of the single airfoil wake. The vortex locations have been noticeably altered and depend on the hindfoil phase. In the near-field wake there is significant vortex interference as closely spaced vortices of opposite sign intrude upon one another. The wake in this region is highly disorganized making it difficult to track changes between phases. However, as the vortices progress downstream, only the dominant structures remain and it becomes notably easier to study the evolution of a particular vortex through the various phases. For example, in Fig. 9 the negative vortex at $x = -435$ mm appears to remain unchanged for phases $\Phi = 0°$ to 180°, however, at $\Phi = 225°$ it splits into 3 distinct structures before collapsing back into a single vortex at $\Phi = 270°$.
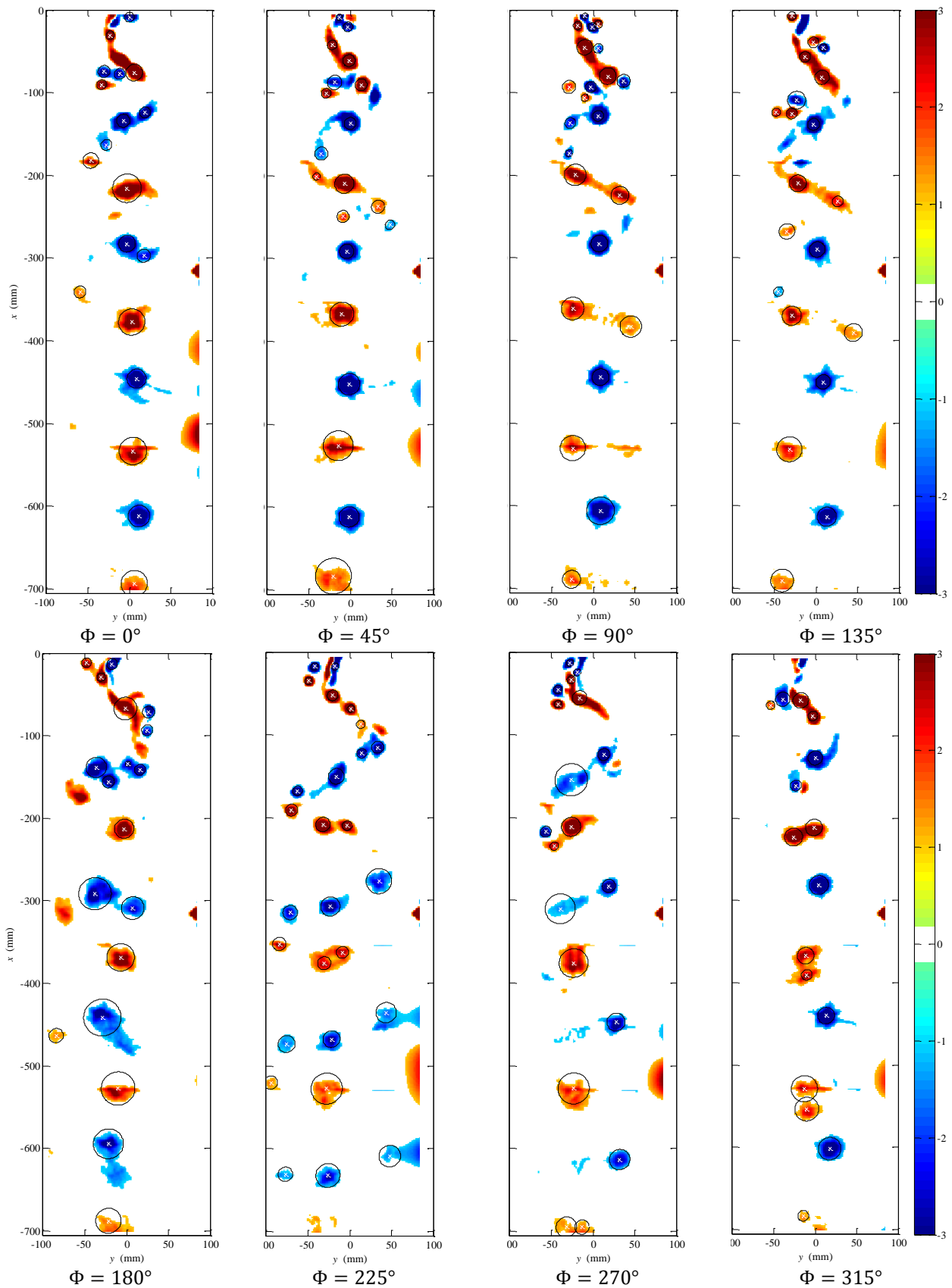
Fig. 9 Vorticity field behind the hindfoil of wake type A for 8 phases $\Phi = 0° - 315°$ with detected vortex cores plotted as white x's and boundary radii as black circles. The circulation Γ $\left(\frac{mm^2}{s}\right)$ is shown in the colour map.

The total contribution of circulation from all the vortices, computed from (8) is averaged over 100 fields and plotted for each of the phases. This along with a cubic interpolated curve and circulation for the single airfoil case is shown in Fig. 10. The error bars represent two standard deviations in the data. The figure indicates that maximum vortex suppression occurs at phase $\Phi = 270°$, maximum vortex enhancement occurs at $\Phi = 90°$, with a secondary enhancement peak appearing at $\Phi = 180°$. This secondary peak is investigated by examining the single airfoil case. The single airfoil wake in Fig. 7 indicates that, in addition to the stronger trailing edge vortices, weaker leading edge vortices appear in the wake as a result of large oscillation amplitudes [2]. These vortices are created at the leading edge and advect along the sides of the airfoil causing them to be shed at different hindfoil phases than the trailing edge vortices [3]. Our hypothsis is that a given hindfoil phase may enhance the relatively weaker leading edge vortices while a different phase may enhance the stronger trailing edge vortices.
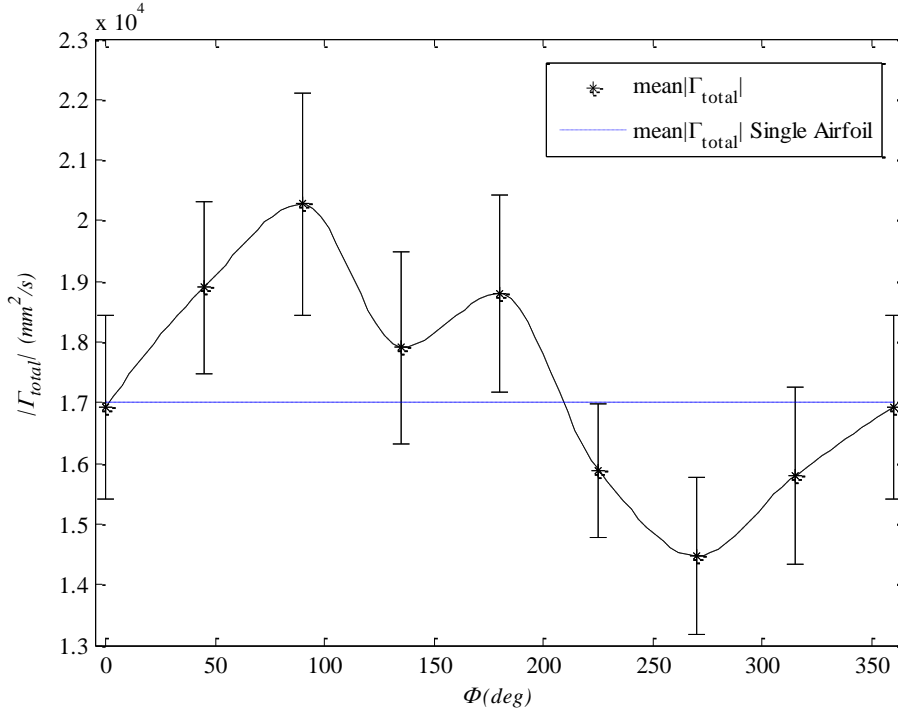

Fig. 10 Total combined circulation from all of the vortices averaged over 100 fields for each phase along with that of the single airfoil case.

For a given set of parameters the CVD algorithm may be identifying a sufficiently high number of weak leading edge vortices which produce two distinct enhancement peaks on the tandem phase diagram as seen in Fig. 10; one corresponding to the strong vortex enhancement phase Φ_{sE} and another for the weak vortex enhancement phase Φ_{wE}. The distinction between weak and strong vortices is determined by observing the single airfoil case and attempting to find a suitable circulation cutoff which would distinguish leading edge vortices from trailing edge ones. The single airfoil wake case shown in Fig. 10 is assumed to be a 2P+2SvK wake. This type of wake is described in [3] by two counter rotating vortices in a von Karman configuration (2S) which are themselves surrounded by a pair of leading edge vortices (2P) for a total of six vortices per oscillation cycle. Investigation of the single airfoil wake reveals that the circulation of the trailing edge (2S) vortices were all well above 500 mm^2/s while that of the leading edge (2P) vortices were well below 500 mm^2/s for our experimental conditions. A suitable circulation cutoff for distinguishing the weak leading edge (2P) vortices from the strong trailing edge (2S) vortices is then $\Gamma_{cut} = 500$ mm^2/s.

Fig. 11 is a tandem phase diagram similar to Fig. 10; however the total circulation $|\Gamma_{total}|$ of only the weak vortices is considered in Fig. 11(a) and only the strong vortices in Fig. 11(b). Fig. 11(a) shows a clear maximum peak at $\Phi = 225°$ and provides evidence supporting the secondary enhancement peak hypothesis. Similarly, in Fig. 11(b), when only the total circulation $|\Gamma_{total}|$ of the strong vortices is considered. The secondary peak at $\Phi = 180°$ seen in Fig. 10 has flattened out and the curve has a well-defined maximum and minimum total circulation at $\Phi = 90°$ and $\Phi = 270°$ respectively.

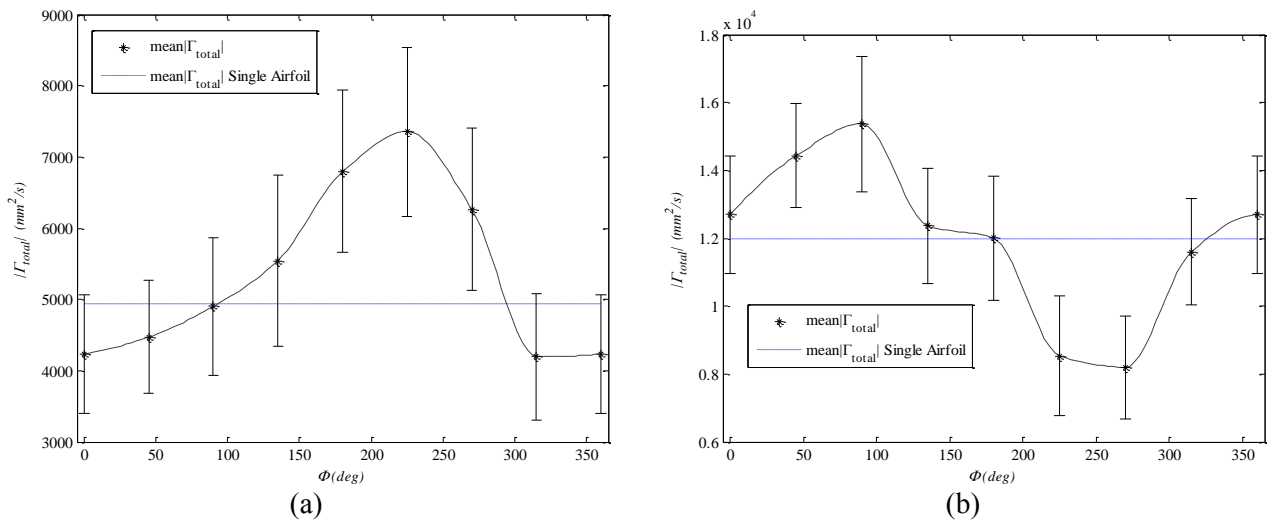Fig. 11 Total combined circulation from all of the (a) weak vortices ($\Gamma \leq 500$ (mm^2/s)) and (b) strong vortices ($\Gamma > 500$ (mm^2/s)) averaged over 100 fields for each phase.

7 Conclusion

Flow visualization and experimental measurement has been used to investigate the vortex field developed behind a single and tandem aerofoil system. The aim of the study has been to develop an understanding of how an aerofoil (hindfoil for the tandem configuration) can be used to affect the vortex wake characteristics of a large-scale vortex structure. This information will be used in future studies to develop an active control system to allow the manipulation of large-scale flow structures. Flow visualization was used to develop a phase map to characterize the different types of vortex configurations that can be generated by a single flapping NACA 0012 aerofoil as a function of flapping amplitude and frequency. PIV was then used to measure the 2D velocity field of a single flapping aerofoil from which vortices were identified and characterized for vortex strength, circulation, size and drift velocity. This was documented as the baseline case for the system for comparison. The velocity and vortex field for a single flapping amplitude and frequency for a tandem arrangement of two NACA 0012 aerofoils was then investigated for different phase differences in flapping frequency. Characterization of the generated flow field showed that vortex properties could be either enhanced or reduced depending on the phase difference between the two aerofoils.

Acknowledgements

References

[1] Jeong J. and Hussain F. (2006) "On the identification of a vortex," *J. Fluid Mech.*, vol. 285, no. −1, p. 69.

[2] Bohl D. G. and Koochesfahani M. M. (2009) "MTV measurements of the vortical field in the wake of an airfoil oscillating at high reduced frequency," *J. Fluid Mech.*, vol. 620, p. 63.

[3] Schnipper T., Andersen A. and Bohr T. (2009) "Vortex wakes of a flapping foil," *J. Fluid Mech.*, vol. 633, p. 411.

[4] Shukla S., Govardhan R. N. and Arakeri J. H. (2009) "Flow over a cylinder with a hinged-splitter plate," *Journal of Fluids and Structures*, vol. 25, no. 4, pp. 713-720.

[5] Gostelow J. P., Platzer M. F., and Carscallen W. E. (2006) "On Vortex Formation in the Wake Flows of Transonic Turbine Blades and Oscillating Airfoils," *Journal of Turbomachinery*, vol. 128, no. 3, p. 528.

[6] Lai J. C. S. and Platzer M. F. (1999) "Jet Characteristics of a Plunging Airfoil," *AIAA Journal*, vol. 37, no. 12, pp. 1529-1537.

[7] Godoy-Diana R., Marais C., Aider J.-L. and Wesfreid J. E. (2009) "A model for the symmetry breaking of the reverse Bénard–von Kármán vortex street produced by a flapping foil," *J. Fluid Mech.*, vol. 622, p. 23.

[8] Vollmers H. (2001), "Detection of vortices and quantitative evaluation of their main parameters from experimental velocity data," *Meas. Sci. Technol*, vol. 12, pp. 1199-1207.

[9] T.L. Hilderman (2004) "Measurement, modelling, and stochastic simulation of concentration fluctuations in a shear flow." PhD. Thesis, The Department of Mechanical Engineering, University of Alberta .

[10] Bussière M.J. (2012) "The experimental investigation of vortex wakes from oscillating airfoils" MSc. Thesis, The Department of Mechanical Engineering, University of Alberta.

[11] M. Raffel, C. Willert, S. Wereley, andJ. Kompenhans, J. (1998). *Particle image velocimetry: A practical guide*. New York, NY: Springer-Verlag

[12] Honkanen, M., and Nobach, H. (2005). Background extraction from double-frame PIV images. *Exp. in Fluids*, 38(3), 348-362.

[13] Brown, D. A. R., Jones, P. N., and Middleton, J. C. (2004). Part A: Measuring tools and techniques for mixing and flow visualization studies. *Handbook of Industrial Mixing*, p. 145-201.

[14] Adrian, R. J., & Westerweel, J. (2011). *Particle Image Velocimetry*. Cambridge University Press.

[15] Madej, A., Babazadeh, H., and Nobes, D. S. (2011). The effect of chamber length and Reynolds number on jet precession. *Exp in Fluids*, 51(6), p. 1623-1643.

[16] Strawn, R. C., Kenwright, N. D., & Ahmad, J. (1999) "Computer visualization of vortex wake systems." *AIAA Journal*, 37(4), p. 511–512.

[17] Portela, L. M. (1997) *Identification and Characterization of Vortices in the Turbulent Boundary Layer.* Ph.D. dissertation, Mech. Eng. Dept., Stanford University.

[18] M.J. Bussière, D.S. Nobes, and C.R. Koch, (2012) "A combinatorial vortex detection and characterization algorithm for 2C2D PIV data", *16th International Symposium on Applications of Laser Techniques to Fluid Mechanics*, Lisbon Portugal, July 9-12, 2012